SEM-EDX Compositional Analysis of Thin Oxide Layers on 316L Stainless Steel for Carbon Nanotube Growth

Alexander Michas

A senior thesis submitted to the faculty of
Brigham Young University
in partial fulfillment of the requirements for the degree of

Bachelor of Science

Felipe Rivera, Advisor

Department of Physics and Astronomy

Brigham Young University

ABSTRACT

SEM-EDX Compositional Analysis of Thin Oxide Layers on 316L Stainless Steel for Carbon Nanotube Growth

Alexander Michas
Department of Physics and Astronomy, BYU
Bachelor of Science

Carbon nanotubes (CNTs) possess exceptional mechanical, electrical, and thermal properties that make them promising for applications including field emission devices, optical collimators, and biofilm-resistant surface coatings. A major challenge in expanding these applications is developing growth methods that are both scalable and compatible with practical engineering substrates. Direct CNT growth on stainless steel is attractive because it avoids the separate catalyst deposition steps typically required in conventional silicon-based methods. In this system, a thin oxide layer formed on the steel surface during oxidation plays a critical role in catalyst formation and subsequent CNT growth. This thesis develops a rapid, accessible method for reliably characterizing the composition of thin oxide layers on 316L stainless steel using scanning electron microscopy with energy dispersive X-ray spectroscopy (SEM-EDX), offering a practical alternative to more time-intensive compositional analysis techniques. Using this method, systematic compositional variations in the oxide were measured across a range of preparation conditions. An increase in manganese, chromium, and iron compared to unoxidized steel was identified and X-ray peak ratios of said elements were quantified, indicating an apparent relative oxidation rate ordering of Mn > Cr > Fe > Ni. These measurements lay the groundwork for future studies correlating oxide characteristics with CNT growth behavior.

Keywords: Carbon Nanotubes, CNT, 316L, Stainless Steel, Oxide, Scale, SEM, EDX, Chemical Vapor Deposition, CVD, CNT growth, catalyst

ACKNOWLEDGMENTS

I would like to thank my advisor, Dr. Felipe Rivera, for his guidance and support throughout this research. I also gratefully acknowledge the BYU Electron Microscopy Facility for providing the instrumentation essential to this work, as well as the BYU College of Computational, Mathematical, and Physical Sciences and the BYU College of Engineering for their support.

Contents

Chapter 1

Introduction

1.1 Carbon Nanotubes and Their Importance

Carbon nanotubes (CNTs) possess several remarkable properties, including extremely high tensile strength, high electrical conductivity, high thermal conductivity, and nanoscale diameter with extremely high aspect ratios. These properties arise from their graphitic bonding and cylindrical geometry, and they make CNTs attractive for a wide range of advanced technological applications. Because CNTs combine structural, electrical, and thermal functionality in a single material system, they are useful both as stand-alone nanostructures and as components in engineered surfaces and devices.

CNTs are actively studied for use in many scientific and industrial technologies. Applications relevant to this thesis include optical collimators [1], bacterial-resistant coatings and implants [2], field emission sources [3], and micro-electro-mechanical systems (MEMS) frameworks [4]. These applications rely on the mechanical, electrical, and structural properties of CNTs.

For CNT-based technologies to be widely implemented, growth methods must be scalable, controllable, and cost-effective. Chemical vapor deposition (CVD) remains the most widely used method for producing CNT forests and coatings because it allows substrate-based growth under tunable thermal and gas-phase conditions. CVD can also accommodate a wide range of substrate materials and geometries, which is important for the practical deployment of CNT-based technologies.

1.2 Catalytic Growth of Carbon Nanotubes

In CVD growth processes, a hydrocarbon precursor gas decomposes at high temperature, carbon dissolves into metal catalyst nanoparticles, excess carbon precipitates from the catalyst particle, and a carbon nanotube forms and grows from the particle [5]. This catalytic model provides the basic framework for understanding CNT synthesis across a wide range of substrates. In the stainless-steel system relevant to this thesis, recent work has shown that oxidized 316L steel can support catalyst formation and subsequent CNT growth through this same general mechanism, with the oxide layer serving as the precursor environment from which catalytic iron nanoparticles emerge [5].

Most CNT growth systems require a deposited metal catalyst layer, catalyst nanoparticle formation during heating, and a substrate that supports the catalyst particles. Common substrates include silicon with deposited alumina barrier layers and iron catalysts. In those conventional systems, iron is intentionally added and alumina is used to isolate and stabilize the catalyst. The oxidized-stainless-steel system studied here is important partly because it can be understood relative to that conventional silicon route, while avoiding the need for a separately deposited catalyst film [5].

Conventional CNT growth systems have several limitations. The catalyst must be deposited separately, additional processing steps increase cost, catalyst layer deposition restricts substrate geometry, and adhesion between CNTs and the substrate can be limited. These limitations are particularly important when CNTs are intended for direct use on industrial or biomedical metal components rather than on idealized silicon wafers [2].

1.3 Direct CNT Growth on Stainless Steel

Stainless steel is an attractive alternative CNT substrate because it contains iron, which serves as the catalyst for CNT growth on steel. In the conventional silicon system, iron is deliberately deposited as the catalyst and alumina is often used as a barrier or support layer. In the oxidized 316L stainless-steel system, chromium appears to play a similar barrier-layer role within the oxide scale. Nickel and manganese are present in the alloy and participate in oxidation behavior, but they play no known direct role in CNT growth on steel in the mechanism emphasized here. This distinction is important because the substrate is not simply catalytic by virtue of containing many alloying elements; rather, the growth mechanism is specifically tied to iron catalyst formation within an oxide environment [5]. Because the steel itself supplies the catalyst, no external deposition step is required, reducing process complexity and cost. Growing CNTs directly on steel also enables strong CNT–substrate adhesion [6] and integration with functional metallic components, advantages not readily available in conventional silicon-based methods. These qualities make stainless steel particularly promising for applications such as field emission devices [3] and biofilm-resistant medical coatings [7].

Although CNTs can grow on untreated stainless steel [8], pretreatment improves growth performance [9]. Methods used in previous studies include polishing, acid etching, sandblasting, and oxidation. Pretreatment affects the near-surface structure from which catalyst particles later form, and therefore it influences CNT morphology and growth quality. Oxidation is especially useful because it can be integrated into the CNT CVD growth process directly. The role of pretreatment and surface nano-features in direct CNT growth on 316 stainless steel has been discussed in [8].

1.4 Oxide Layer Role and Characterization

Exposing stainless steel to oxygen in a CVD process produces a thin (< 200 nm) oxide layer, or scale, on the surface of the steel. This scale is rich in chromium, iron, and manganese oxides. Recent work by the BYU Nanomaterials Research Group has shown that this oxide layer plays a crucial role in CNT growth. Focused ion beam (FIB) cross-sectioning with transmission electron microscopy (TEM) studies have shown that CNTs grow from iron-rich nanoparticles embedded in the oxide layer, and that these nanoparticles form when iron is reduced out of the oxide during exposure to hydrocarbon precursors [5]. Thus, the oxide layer acts as the precursor to CNT catalyst formation. Oxide scale is studied primarily as an industrial byproduct or as something to be mitigated [10]. Consequently, the short oxidation times (< 10 minutes) relevant in this thesis have not been previously studied.

Although high-resolution interface methods provide detailed information, they require extensive preparation, including protective atomic layer deposition (ALD) coatings, FIB milling and lamella extraction, and TEM imaging and spectroscopy. Analyzing a single sample with these techniques can require multiple days of work. Characterizing the oxide across many conditions requires a method that is much more efficient. This thesis develops a fast and reliable method using scanning electron microscopy (SEM) with energy dispersive X-ray spectroscopy (EDX) to measure comparative oxide composition across a wide range of oxidation conditions.

1.5 Experimental Pipeline

The experimental workflow consists of three stages: sample preparation, oxidation, and SEM-EDX characterization. 316L stainless steel samples are cut from a larger sheet into $\sim$1 cm^2 tiles. These samples are placed in a CVD furnace and heated to temperatures ranging from 600 to 900°C while exposed to air flowing at 371 sccm for times ranging from 0.5 to 4 minutes, forming a thin (< 200 nm) oxide scale on the steel surface. The oxidized samples are then studied in a Helios Nanolab 600 SEM equipped with EDX analysis and FIB capabilities. A high-angle 80° tilt is used to increase electron beam exposure of the thin oxide layer, improving the X-ray signal from the region of interest relative to the bulk substrate. EDX spectra are collected and normalized to the Fe K_α peak, and comparative peak-ratio analysis is used to identify compositional changes across oxidation conditions. FIB milling is also used to expose the bulk substrate beneath the oxide, providing control spectra for comparison.

The results reveal systematic compositional trends across oxidation conditions, including changes in Ni/Fe, Cr/Fe, Ni/Cr and Cr/Mn ratios with temperature and time, demonstrating that SEM-EDX can reliably distinguish between oxide layers formed under different preparation parameters. Future work will correlate these oxide composition measurements with CNT growth morphology and adhesion to establish direct links between oxidation conditions and CNT properties.

Chapter 2

Methods and Experimental Design

2.1 Sample Preparation

The substrate material used in this thesis was 316L stainless steel. Samples were cut into approximately 1 cm^2 chips prior to oxidation and CNT growth experiments. This material was selected because it supports direct CNT growth following oxidation and because its alloy composition gives rise to a thin multi-element oxide scale relevant to catalyst formation.

Samples were oxidized in a CVD furnace. Oxidation parameters included temperatures from 600 to 900 °C, times from 0.5 to 4 minutes, and flowing air as the oxidizing gas. After oxidation, the furnace was purged with argon and the samples were cooled under argon flow. These oxidation conditions were chosen to generate thin oxide layers, such as the one seen in Fig. 2.1a, suitable both for SEM-EDX characterization and for CNT growth studies [11].

2.2 Oxide Scale Characterization

SEM imaging was used to reveal the microstructure of the oxide layer. Surface imaging provides a top-view representation of the oxidized steel surface and allows qualitative assessment of oxide

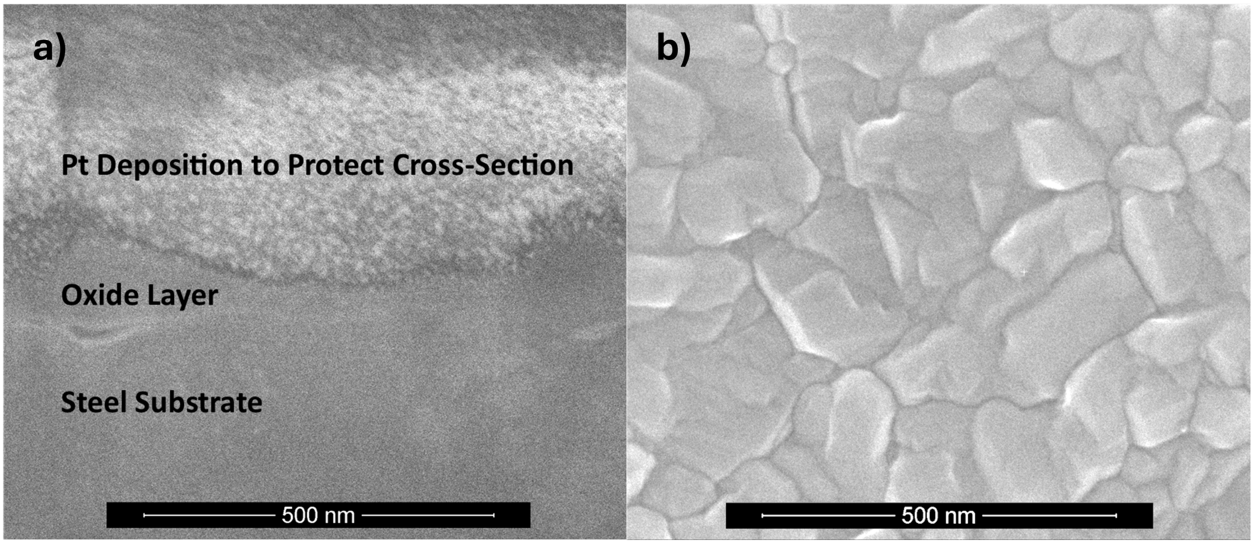

Figure 2.1 a) Vertical cross section of a thin (50–200 nm) oxide layer. Sample oxidized at 900 °C for 4 minutes. b) Oxide grains visible on the surface of 316L stainless steel. Sample oxidized at 750 °C for 4 minutes.

grains and surface texture prior to CNT growth (Fig. 2.1b). This information is important because the oxide surface is the environment from which catalytic nanoparticles later emerge.

Samples were analyzed using a dual-beam FIB/SEM system. For FIB and EDX work, the primary instrument was a FEI Helios NanoLab 600 DualBeam FIB/SEM. General imaging associated with this thesis also used the FEI Helios NanoLab 600 DualBeam FIB/SEM, Verios G4 UC SEM, and Apreo C SEM. An electron beam energy of 15 keV was used as the standard accelerating voltage across measurements. Samples were tilted to an angle of 80° to maximize the interaction between the electron beam and the thin oxide layer. A graphic representation of the SEM sample chamber geometry is shown in Fig. 2.2a. Reliable compositional results would be impossible to obtain without this sample configuration. X-rays emitted by Cr, Mn, Fe, and Ni were collected for EDX analysis [11].

Control spectra were obtained by removing the oxide layer with the FIB. The FIB was used to mill away the surface scale locally so that EDX spectra could be acquired from the exposed bulk steel beneath (Fig. 2.2b). These control spectra provide a baseline for comparison with spectra

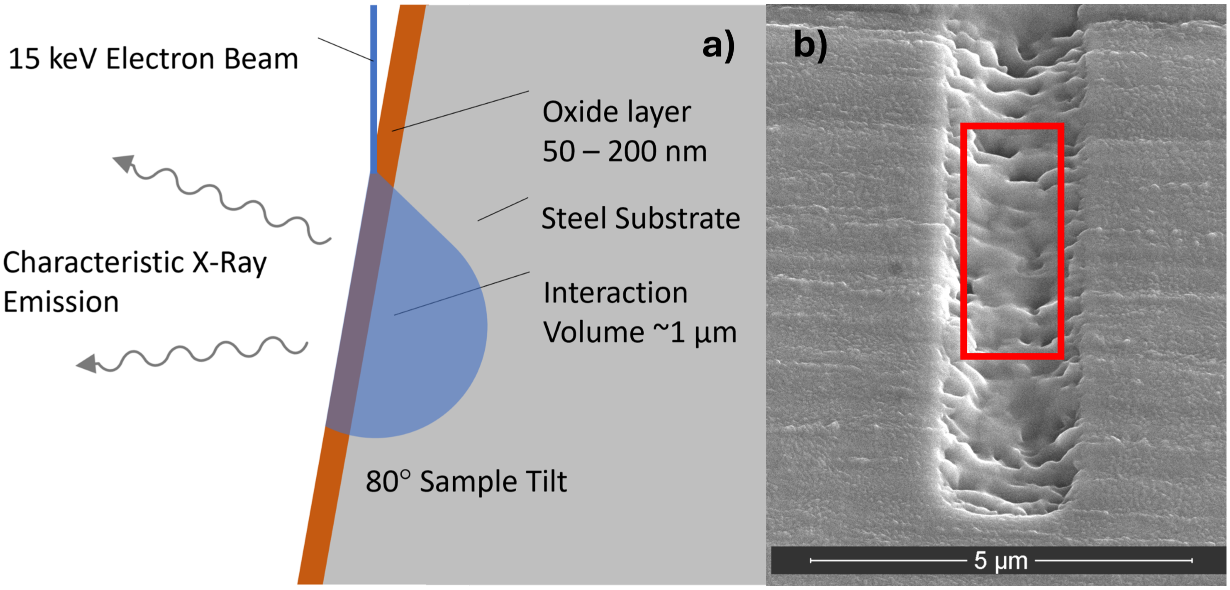

Figure 2.2 a) Sample configuration inside SEM. Electron beam energy was set to 15 keV to excite X-ray peaks of interest (Cr, Mn, Fe, & Ni). X-rays are collected for EDX analysis. High angle 80° sample tilt increases the amount of the electron beam interaction volume occupied by the oxide layer (the region of interest). b) An oxidized 316L stainless steel sample with a portion of the oxide layer milled away by the FIB. The EDX spectrum from the region outlined in red represents the bulk steel composition and was used as the control measurement.

obtained from oxidized surfaces and help distinguish quantitative changes in the oxide layer from bulk substrate composition. Control spectra from multiple samples were taken and found to be indistinguishable both from each other and from untreated 316L stainless steel, confirming the reliability of the control measurement.

2.3 EDX Spectra Analysis

When excited by the electron beam, each element in the sample emits X-rays at characteristic energies. These X-rays are collected by a solid state detector and recorded as a histogram of detected counts in 5 eV energy bins. Example spectra from four oxidation conditions are shown in Fig. 2.3. Several X-ray peaks are present in the spectra of oxidized stainless steel. While peak height is not directly characteristic of elemental mass ratios, changes in relative peak intensities reflect quantitative changes in elemental concentrations across samples. In this thesis, EDX analysis is treated as semi-quantitative and peak-ratio-based rather than fully quantitative. The large region of interest ($\sim$10 μm^2) and 2-minute acquisition time provided adequate sampling of each surface and made multiple spectra per sample unnecessary. The general analysis goal was to extract relative quantitative relationships in surface composition across oxidation conditions rather than absolute atomic percentages.

To accomplish this, ratios between X-ray peaks from different elements were calculated and plotted across oxidation conditions. Ratios analyzed include Ni/Fe, Cr/Fe, Ni/Cr, and Cr/Mn; these ratios were selected because they compare all of the elements of interest and have a strong signal-to-noise ratio. Several steps are required to process the EDX histogram data into a usable format. The Mathematica script in Appendix A was written to streamline the process of contour plot creation, automating steps such as removing background X-ray signals, cropping spectra peaks, combining multiple spectra, and assigning samples to positions on the plots, reducing the data

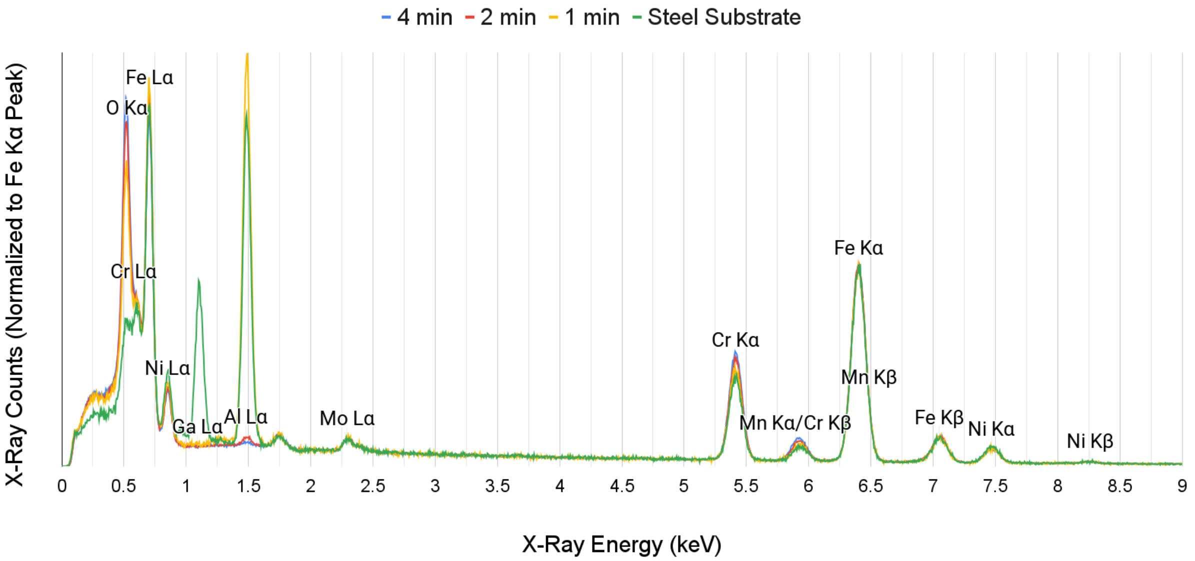

Figure 2.3 EDX spectra (normalized to Fe K_α) for stainless steel samples oxidized at 750 °C for 1, 2, and 4 minutes, with a FIB-exposed bulk substrate control. Note the increase in the Cr K_α peak with oxidation time, indicating a higher Cr/Fe ratio at longer oxidation times. While difficult to visualize without further analysis, Mn and Ni also have variations in their peaks. The Al peak is attributed to background from the sample holder and the Ga peak to residual FIB ion implantation.

processing time per sample to seconds. All that is now required of the user is correct use of the `PlotCharts` function and a correct folder structure.

Chapter 3

Results

3.1 Oxide Scale Characterization Results

EDX analysis revealed systematic compositional trends across oxidation conditions. The contour plots in Fig. 3.1 map oxide composition across the experimental oxidation parameter space using oxidation temperature and oxidation time as the axes. A dimensionless ratio value is used to reflect the composition of the oxide relative to the control measurement. Observed changes in oxide composition include an increase in Cr/Fe ratio with oxidation duration and temperature, a decrease in Ni/Fe ratio, and a decrease in Cr/Mn ratio. These trends indicate differential oxidation and diffusion of alloying elements in the thin oxide scale.

The relative oxidation or diffusion behavior inferred from the oxide data is: Mn $>$ Cr $>$ Fe $>$ Ni. This ordering is consistent with the later-stage oxidation behavior identified in studies of steel oxides formed under long time durations [10]. It also reflects the fact that manganese and chromium enrich the surface oxide more readily than iron, while nickel remains comparatively depleted from the oxide scale.

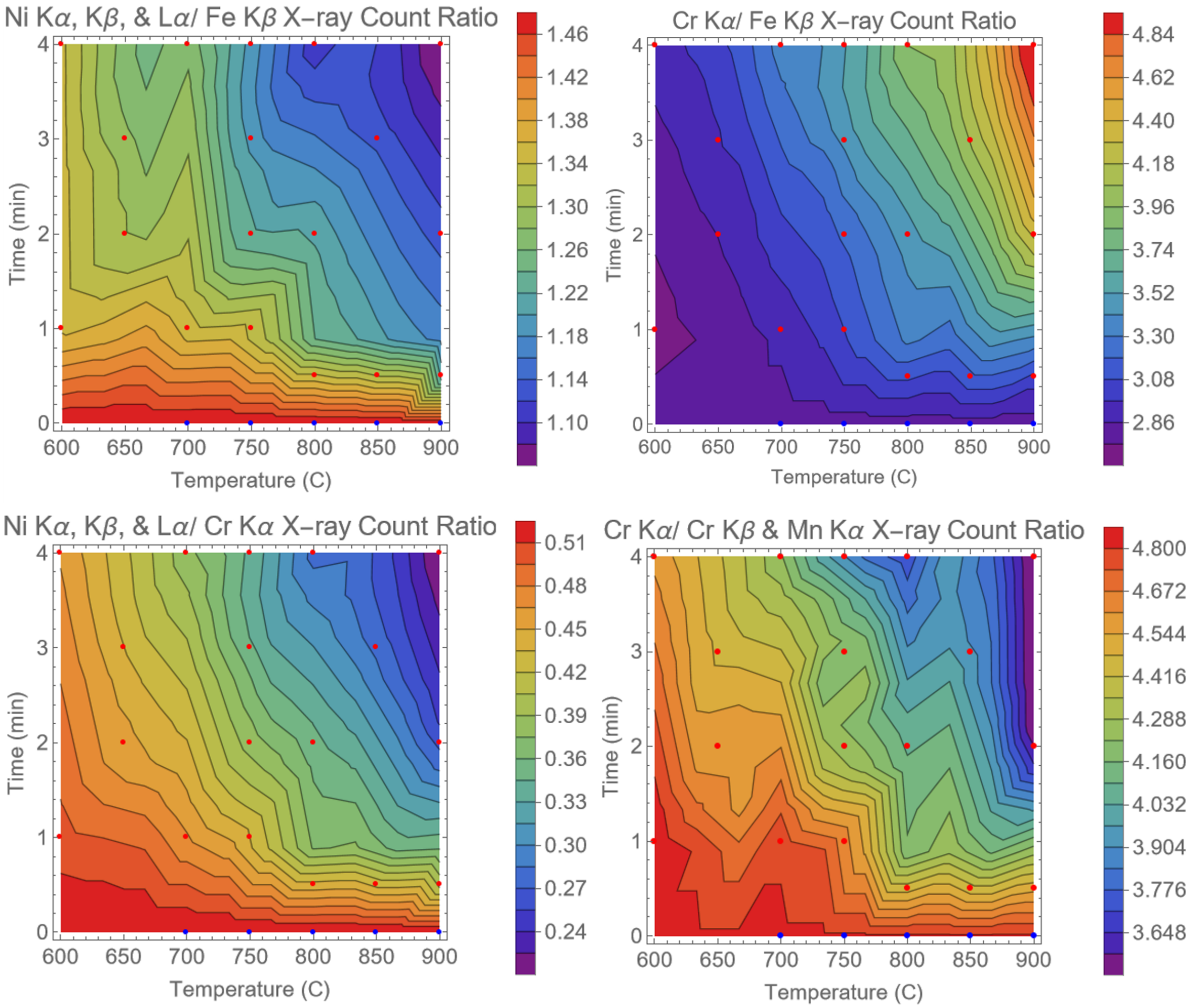

Figure 3.1 Contour plots to illustrate X-ray count ratios between elements of interest (Cr, Mn, Fe, and Ni) across sample preparation time and temperature. Specific X-ray peaks used in the ratio are indicated in the title of each plot and can be identified in Fig. 2.3. Red dots are measured data points. Blue dots on the x-axis indicate the control measurement taken with the method in Fig. 2.2b.

Most oxidation studies examine time scales of hours, days, or months. In contrast, this work studies oxidation times of only minutes. Early-stage oxidation on the time scale relevant to CNT preparation has now been reliably characterized semi-quantitatively.

Chapter 4

Discussion and Conclusions

4.1 Oxide Formation Behavior

Thermal oxidation of 316L stainless steel under the short time scales used in this thesis produced thin oxide layers composed primarily of chromium, manganese, iron, and nickel oxides. SEM-EDX analysis revealed systematic changes in elemental ratios as a function of oxidation temperature and time. In particular, the Cr/Fe ratio increased with oxidation duration and temperature, while the Ni/Fe ratio decreased and the Cr/Mn ratio decreased. These reflect the relative diffusion and oxidation behavior of the alloying elements present in 316L stainless steel and are consistent with trends measured over much longer oxidation times [10], corroborating the reliability of this method's ability to detect changes in oxide composition.

Chromium enrichment within the oxide layer is consistent with its tendency to form stable oxide phases that act as protective barriers. Manganese, which exhibits higher diffusivity, appears to migrate toward the surface more rapidly during early oxidation, an unexpected result compared to the previous study of the oxide catalyst layer [5]. Nickel shows limited participation in oxide formation and remains largely in the bulk metal.

4.2 Catalyst Formation Within the Oxide Layer

The oxide layer formed during oxidation plays a central role in CNT growth by acting as the precursor structure for catalyst particle formation. During CNT growth, exposure to hydrocarbon gases leads to the reduction of iron within the oxide layer and the formation of iron-rich nanoparticles embedded within the oxide matrix. These nanoparticles serve as catalytic sites for CNT nucleation and growth [5]. The composition of the oxide layer therefore directly influences catalyst formation. Variations in chromium, manganese, and iron concentrations may affect:

- availability of iron for catalyst formation
- diffusion of iron within the oxide layer
- catalyst particle size and density
- catalyst stability during growth

Chromium-rich oxide environments may act as barrier layers that restrict diffusion, while manganese-rich regions may influence early-stage oxide restructuring. Because catalyst particles originate from iron within the oxide, changes in oxide composition are expected to directly influence CNT growth behavior.

4.3 Oxide Composition as a CNT Growth Meta-Parameter

Although CNT growth is typically described in terms of experimental parameters such as temperature and time, these variables influence CNT formation indirectly through their effect on oxide composition.

In this work, oxidation temperature and time determine the composition of the oxide layer, which in turn governs catalyst formation and CNT growth. From this perspective, oxide composition functions as a *meta-parameter* linking preparation conditions to CNT properties.

This framework allows CNT growth behavior to be interpreted in terms of underlying material structure rather than purely empirical growth conditions. By focusing on oxide composition, it becomes possible to develop more predictive models of CNT growth on stainless steel substrates.

4.4 Role of SEM-EDX in Future CNT Growth Studies

Traditional high-resolution techniques such as FIB/TEM provide detailed information about the CNT–substrate interface but require extensive sample preparation and analysis time, often taking days. In contrast, SEM-EDX provides a rapid and largely non-destructive method for analyzing oxide composition. Measurements can be completed in minutes per sample, enabling systematic studies across a wide parameter space. Although SEM-EDX does not provide fully quantitative elemental composition for very thin oxide layers, it reliably detects relative compositional changes between samples when measurements are performed consistently.

The results of this thesis demonstrate that this SEM-EDX procedure is sufficient to characterize oxide layers relevant to CNT growth. This capability opens several directions for future work. The oxide composition data collected here can be correlated with CNT width, length, and surface density to determine how preparation conditions influence CNT morphology through the oxide meta-parameter. Because CNTs are rooted in and adhere to the oxide layer, understanding how oxide composition affects the strength and mechanism of CNT-oxide adhesion is similarly important for developing durable CNT coatings. Together, these future studies would make SEM-EDX a powerful tool for systematically optimizing CNT growth on metallic substrates.

Appendix A

Mathematica Script

Listing A.1 Mathematica script for EDX contour plot generation.

```
(*Assumes that .csv histgram files are sorted into 5 eV buckets, Column 1 being
    bucket label, and Column 2 being X-ray count number*)
SetDirectory[NotebookDirectory[]];
CrFeRatio[filename_] :=
 Module[{name = filename},
  rawSpec = Import[name];
  rawSpec[[1]] = {1, 1};

  bg = Fit[
    Join[rawSpec[[600 ;; 1025]], rawSpec[[1160 ;; 1185]],
     rawSpec[[1340 ;; 1360]], rawSpec[[1550 ;; 1600]],
     rawSpec[[1950 ;; 4000]]], {1, 1/x}, x];

  bglist = bg /. x -> Transpose[rawSpec][[1]];
  spec = Transpose[rawSpec][[2]] - bglist;
```

```
  crcontent = Total[spec[[1025 ;; 1135]]];
  fecontent = Total[spec[[1350 ;; 1460]]];
  crferatio = crcontent/fecontent // N;
  Return[crferatio];
  ]

CrPeakRatioMn[filename_] :=
 Module[{name = filename},
  rawSpec = Import[name];
  rawSpec[[1]] = {1, 1};

  bg = Fit[
    Join[rawSpec[[600 ;; 1025]], rawSpec[[1160 ;; 1185]],
     rawSpec[[1340 ;; 1360]], rawSpec[[1550 ;; 1600]],
     rawSpec[[1950 ;; 4000]]], {1, 1/x}, x];

  bglist = bg /. x -> Transpose[rawSpec][[1]];
  spec = Transpose[rawSpec][[2]] - bglist;

  crP1content = Total[spec[[1045 ;; 1135]]];
  crP2content = Total[spec[[1135 ;; 1228]]];
  crPratio = crP1content/crP2content // N;
  Return[crPratio];
  ]

FePeakRatioMn[filename_] :=
```

```
 Module[{name = filename},
  rawSpec = Import[name];
  rawSpec[[1]] = {1, 1};

  bg = Fit[
    Join[rawSpec[[600 ;; 1025]], rawSpec[[1160 ;; 1185]],
     rawSpec[[1340 ;; 1360]], rawSpec[[1550 ;; 1600]],
     rawSpec[[1950 ;; 4000]]], {1, 1/x}, x];

  bglist = bg /. x -> Transpose[rawSpec][[1]];
  spec = Transpose[rawSpec][[2]] - bglist;

  feP1content = Total[spec[[1228 ;; 1350]]];
  feP2content = Total[spec[[1350 ;; 1455]]];
  fePratio = feP1content/feP2content // N;
  Return[fePratio];
  ]

NiFeRatioWLa[filename_] :=
 Module[{name = filename},
  rawSpec = Import[name];
  rawSpec[[1]] = {1, 1};

  bg = Fit[
    Join[rawSpec[[600 ;; 1025]], rawSpec[[1160 ;; 1185]],
     rawSpec[[1340 ;; 1360]], rawSpec[[1550 ;; 1600]],
     rawSpec[[1950 ;; 4000]]], {1, 1/x}, x];
```

```
  bg2 = Fit[
    Join[rawSpec[[156 ;; 159]], rawSpec[[189 ;; 201]]], {1, 1/x}, x];

  bglist = bg /. x -> Transpose[rawSpec][[1]];
  bg2list = bg2 /. x -> Transpose[rawSpec][[1]];
  spec = Transpose[rawSpec][[2]] - bglist;
  spec2 = Transpose[rawSpec][[2]] - bg2list;

  nicontent = Total[spec[[1461 ;; 1710]]] + Total[spec2[[160 ;; 188]]];
  fecontent = Total[spec[[1350 ;; 1460]]];
  niferatio = nicontent/fecontent // N;
  Return[niferatio];
  ]

NiFeRatio[filename_] :=
 Module[{name = filename},
  rawSpec = Import[name];
  rawSpec[[1]] = {1, 1};

  bg = Fit[
    Join[rawSpec[[600 ;; 1025]], rawSpec[[1160 ;; 1185]],
     rawSpec[[1340 ;; 1360]], rawSpec[[1550 ;; 1600]],
     rawSpec[[1950 ;; 4000]]], {1, 1/x}, x];
  bg2 = Fit[
    Join[rawSpec[[156 ;; 159]], rawSpec[[189 ;; 201]]], {1, 1/x}, x];

  bglist = bg /. x -> Transpose[rawSpec][[1]];
```

```
  spec = Transpose[rawSpec][[2]] - bglist;

  nicontent = Total[spec[[1461 ;; 1710]]];
  fecontent = Total[spec[[1350 ;; 1460]]];
  niferatio = nicontent/fecontent // N;
  Return[niferatio];
  ]

NiCrRatioWLa[filename_] :=
 Module[{name = filename},
  rawSpec = Import[name];
  rawSpec[[1]] = {1, 1};

  bg = Fit[
    Join[rawSpec[[600 ;; 1025]], rawSpec[[1160 ;; 1185]],
     rawSpec[[1340 ;; 1360]], rawSpec[[1550 ;; 1600]],
     rawSpec[[1950 ;; 4000]]], {1, 1/x}, x];
  bg2 = Fit[
    Join[rawSpec[[156 ;; 159]], rawSpec[[189 ;; 201]]], {1, 1/x}, x];

  bglist = bg /. x -> Transpose[rawSpec][[1]];
  bg2list = bg2 /. x -> Transpose[rawSpec][[1]];
  spec = Transpose[rawSpec][[2]] - bglist;
  spec2 = Transpose[rawSpec][[2]] - bg2list;

  nicontent = Total[spec[[1461 ;; 1710]]] + Total[spec2[[160 ;; 188]]];
  crcontent = Total[spec[[1025 ;; 1135]]];
```

```
  nicrratio = nicontent/crcontent // N;
  Return[nicrratio];
  ]

PlotCharts[plotrange_, filelist_, anchorfile_, anchorpoints_] :=
 Module[{datalist = filelist, range = plotrange, afile = anchorfile,
   apoints = anchorpoints},
  tdata = Transpose[datalist];

  CrFeSubstrate = CrFeRatio[afile];
  NiFeSubstrate = NiFeRatio[afile];
  NiFeWLaSubstrate = NiFeRatioWLa[afile];
  NiCrWLaSubstrate = NiCrRatioWLa[afile];

  CrPeakSubstrate = CrPeakRatioMn[afile];
  FePeakSubstrate = FePeakRatioMn[afile];

  axispoints = apoints;

  CrFeAxes = Append[CrFeSubstrate] /@ axispoints;
  NiFeAxes = Append[NiFeSubstrate] /@ axispoints;
  NiFeWLaAxes = Append[NiFeWLaSubstrate] /@ axispoints;
  NiCrWLaAxes = Append[NiCrWLaSubstrate] /@ axispoints;

  CrPeakAxes = Append[CrPeakSubstrate] /@ axispoints;
  FePeakAxes = Append[FePeakSubstrate] /@ axispoints;
```

```
CrFeTdata = Join[tdata[[1 ;; 2]], {CrFeRatio[#] & /@ tdata[[3]]}];
NiFeTdata = Join[tdata[[1 ;; 2]], {NiFeRatio[#] & /@ tdata[[3]]}];
NiFeWLaTdata =
 Join[tdata[[1 ;; 2]], {NiFeRatioWLa[#] & /@ tdata[[3]]}];
NiCrWLaTdata =
 Join[tdata[[1 ;; 2]], {NiCrRatioWLa[#] & /@ tdata[[3]]}];

CrPeakdata =
 Join[tdata[[1 ;; 2]], {CrPeakRatioMn[#] & /@ tdata[[3]]}];
FePeakdata =
 Join[tdata[[1 ;; 2]], {FePeakRatioMn[#] & /@ tdata[[3]]}];

{CrFeTdata, NiFeTdata, NiFeWLaTdata, NiCrWLaTdata, CrPeakdata,
  FePeakdata} =
 Transpose[#] & /@ {CrFeTdata, NiFeTdata, NiFeWLaTdata,
   NiCrWLaTdata, CrPeakdata, FePeakdata};

CrFeTdata = Join[CrFeAxes, CrFeTdata];
NiFeTdata = Join[NiFeAxes, NiFeTdata];
NiFeWLaTdata = Join[NiFeWLaAxes, NiFeWLaTdata];
NiCrWLaTdata = Join[NiCrWLaAxes, NiCrWLaTdata];

CrPeakdata = Join[CrPeakAxes, CrPeakdata];
FePeakdata = Join[FePeakAxes, FePeakdata];

{CrFePlot, NiFePlot, NiFeWLaPlot, NiCrWLaPlot, CrPeakPlot,
  FePeakPlot} = ListContourPlot[#,
```

```
    PlotRange ->
     If[range === All, All,
      Join[range, {{Min[Transpose[#][[3]]],
         Max[Transpose[#][[3]]]}}]], ImageSize -> Medium,
    PlotLegends -> Automatic, ColorFunction -> "Rainbow",
    Contours -> 20, MaxPlotPoints -> 10,
    FrameLabel -> {"Temperature␣(C)",
      "Time␣(min)"}] & /@ {CrFeTdata, NiFeTdata, NiFeWLaTdata,
   NiCrWLaTdata, CrPeakdata, FePeakdata};

{CrFePlot3D, NiFePlot3D, NiFeWLaPlot3D, NiCrWLaPlot3D, CrPeakPlot3D,
   FePeakPlot3D} = ListPlot3D[#,
    PlotRange -> range, ImageSize -> Medium,
    PlotLegends -> Automatic, ColorFunction -> "Rainbow",
    ViewPoint -> {-5, -20, 15},
    AxesLabel -> {"Temperature␣(C)", "Time␣(min)"},
    AxesEdge -> {Automatic, {-1, -1}, None}] & /@ {CrFeTdata,
   NiFeTdata, NiFeWLaTdata, NiCrWLaTdata, CrPeakdata, FePeakdata};

dataplot =
 ListPlot[tdata[[1 ;; 2]] // Transpose, PlotStyle -> Red];
dataplot3d = ListPointPlot3D[tdata // Transpose, PlotStyle -> Red];
axisplot = ListPlot[axispoints, PlotStyle -> Blue];

Export["CrFePlot.png",
 Show[CrFePlot, dataplot, axisplot,
  PlotLabel -> "Cr␣K\[Alpha]/␣Fe␣K\[Beta]␣X-ray␣Count␣Ratio"]];
```

```
  Export["NiFeWLaPlot.png",
   Show[NiFeWLaPlot, dataplot, axisplot,
    PlotLabel ->
     "Ni␣K\[Alpha],␣K\[Beta],␣&␣L\[Alpha]/␣Fe␣K\[Beta]␣X-ray␣Count␣\
Ratio"]];
  Export["NiCrWLaPlot.png",
   Show[NiCrWLaPlot, dataplot, axisplot,
    PlotLabel ->
     "Ni␣K\[Alpha],␣K\[Beta],␣&␣L\[Alpha]/␣Cr␣K\[Alpha]␣X-ray␣Count␣\
Ratio"]];
  Export["CrPeakPlot.png",
   Show[CrPeakPlot, dataplot, axisplot,
    PlotLabel ->
     "Cr␣K\[Alpha]/␣Cr␣K\[Beta]␣&␣Mn␣K\[Alpha]␣X-ray␣Count␣Ratio"]];


  {{Show[CrFePlot, dataplot, axisplot,
     PlotLabel -> "Cr␣K\[Alpha]/␣Fe␣K\[Beta]␣X-ray␣Count␣Ratio"],
    Show[CrFePlot3D, dataplot3d,
     PlotLabel -> "Cr␣K\[Alpha]/␣Fe␣K\[Beta]␣X-ray␣Count␣Ratio"]},
   {Show[NiFeWLaPlot, dataplot, axisplot,
     PlotLabel ->
      "Ni␣K\[Alpha],␣K\[Beta],␣&␣L\[Alpha]/␣Fe␣K\[Beta]␣X-ray␣Count␣\
Ratio"],
    Show[NiFeWLaPlot3D, dataplot3d,
     PlotLabel ->
      "Ni␣K\[Alpha],␣K\[Beta],␣&␣L\[Alpha]/␣Fe␣K\[Beta]␣X-ray␣Count␣\
Ratio"]},
```

```
   {Show[NiCrWLaPlot, dataplot, axisplot,
     PlotLabel ->
      "Ni␣K\[Alpha],␣K\[Beta],␣&␣L\[Alpha]/␣Cr␣K\[Alpha]␣X-ray␣Count␣\
Ratio"],
    Show[NiCrWLaPlot3D, dataplot3d,
     PlotLabel ->
      "Ni␣K\[Alpha],␣K\[Beta],␣&␣L\[Alpha]/␣Cr␣K\[Alpha]␣X-ray␣Count␣\
Ratio"]},
   {Show[CrPeakPlot, dataplot, axisplot,
     PlotLabel ->
      "Cr␣K\[Alpha]/␣Cr␣K\[Beta]␣&␣Mn␣K\[Alpha]␣X-ray␣Count␣Ratio"],
    Show[CrPeakPlot3D, dataplot3d,
     PlotLabel ->
      "Cr␣K\[Alpha]/␣Cr␣K\[Beta]␣&␣Mn␣K\[Alpha]␣X-ray␣Count␣Ratio"]},
   {Show[FePeakPlot, dataplot, axisplot,
     PlotLabel ->
      "Fe␣K\[Alpha]␣&␣Mn␣K\[Beta]/␣Fe␣K\[Beta]␣X-ray␣Count␣Ratio"],
    Show[FePeakPlot3D, dataplot3d,
     PlotLabel ->
      "Fe␣K\[Alpha]␣&␣Mn␣K\[Beta]/␣Fe␣K\[Beta]␣X-ray␣Count␣Ratio"]}}
  ]


{Show[NiFePlot, dataplot, axisplot,
   PlotLabel ->
    "Ni/Fe␣X-ray␣Count␣Ratio␣(from␣K\[Alpha]␣&␣K\[Beta]␣peaks)"],
  Show[NiFePlot3D, dataplot3d,
   PlotLabel ->
```

```
    "Ni/Fe␣X-ray␣Count␣Ratio␣(from␣K\[Alpha]␣&␣K\[Beta]␣peaks)"]};


-------------------------------------------------------------------


PlotCharts[{(*Plot Boundaries: {Min Temp,Max Temp},{Min Time,
  Max Time}}*){600, 900}, {0, 4}},
 (*Use convention: {Temperature (C), Time (min), File name (place \
.csv files in notebook directory)}*)
 {{600, 1, "A46␣Pre-FIB␣80␣Tilt.csv"},
  {600, 4, "A11␣Pre-FIB␣80␣Tilt.csv"},
  {650, 2, "650␣C␣2␣min.csv"},
  {650, 3, "650␣C␣3␣min.csv"},
  {700, 1, "A43␣Pre-FIB.csv"},
  {700, 4, "A3␣Pre-FIB␣80␣Tilt.csv"},
  {750, 1, "A19␣Pre-FIB␣80␣Tilt.csv"},
  {750, 2, "A18␣Pre-FIB␣80␣Tilt.csv"},
  {750, 3, "750␣C␣3␣min.csv"},
  {750, 4, "A17␣Pre-FIB␣80␣Tilt␣47%␣DT.csv"},
  {800, 16, "J␣800␣16␣Pre-FIB␣80␣Tilt.csv"},
  {800, 8, "J␣800␣8␣Pre-FIB␣80␣Tilt.csv"},
  {800, 4, "J␣800␣4␣Pre-FIB␣SEM2␣80␣Tilt.csv"},
  {800, 2, "J␣800␣2␣Pre-FIB.csv"},
  {800, .5, "A10␣Pre-FIB␣80␣Tilt.csv"},
  {850, .5, "Manual␣850␣C␣.5␣min␣Interpolation.csv"},
  {850, 3, "850␣C␣3␣min.csv"},
  {900, .5, "A45␣Pre-FIB␣80␣Tilt.csv"},
  {900, 2, "A44␣Pre-FIB␣80␣Tilt.csv"},
```

```
 {900, 4, "A42␣Pre-FIB.csv"}},
"Steel␣Substrate␣Average.csv",
{{0, 0}, {0, 16}, {700, 0}, {900, 0}, {850, 0}, {750, 0}, {800, 0}}]
```

Bibliography

[1] S. C. Olsen, D. D. Allred, and R. R. Vanfleet, “Carbon nanotube collimator as an vacuum ultraviolet window,” Journal of Vacuum Science & Technology B **42,** 043001 (2024).

[2] S. R. Morco, D. L. Williams, B. D. Jensen, and A. E. Bowden, “Structural biofilm resistance of carbon-infiltrated carbon nanotube coatings,” Journal of Orthopaedic Research **40,** 1953–1960 (2022).

[3] S. C. Olsen, B. Vandyke, R. R. Vanfleet, and V. Robinson, “Field emission from flipped and patterned vertically aligned carbon nanotube arrays,” Nanotechnology **36,** 075703 (2024).

[4] D. N. Hutchison, N. B. Morrill, Q. Aten, B. W. Turner, B. D. Jensen, L. L. Howell, R. R. Vanfleet, and R. C. Davis, “Carbon Nanotubes as a Framework for High-Aspect-Ratio MEMS Fabrication,” Journal of Microelectromechanical Systems **19,** 75–82 (2010).

[5] J. D. Hancock, A. K. Michas, B. D. Jensen, F. Rivera, and R. R. Vanfleet, “Mechanisms for carbon nanotube growth on oxidized 316L stainless steel substrates,” Applied Surface Science **710,** 163993 (2025).

[6] A. Michas, T. Germany, F. Rivera, B. Jensen, and R. Vanfleet, “Adhesive Strength of Carbon Nanotubes Grown on Various Substrates,” Microscopy and Microanalysis **31,** 1901–1903 (2025).

[7] S. R. Morco, “Characterizing Bacterial Resistance and Microstructure-Related Properties of Carbon-Infiltrated Carbon Nanotube Surface Coatings with Applications in Medical Devices,” Ph.D. dissertation, Brigham Young University (2021).

[8] M. Hashempour, A. Vicenzo, F. Zhao, and M. Bestetti, “Direct growth of MWCNTs on 316 stainless steel by chemical vapor deposition: Effect of surface nano-features on CNT growth and structure,” Carbon **63,** 330–347 (2013).

[9] C. Zhuo, X. Wang, W. Nowak, and Y. A. Levendis, “Oxidative heat treatment of 316L stainless steel for effective catalytic growth of carbon nanotubes,” Applied Surface Science **313,** 227–236 (2014).

[10] T. Zheng and J. T. Han, “High temperature oxidation behavior of SUS310S austenitic stainless steel,” Advanced Materials Research **941-944,** 212–215 (2014).

[11] A. Michas, F. Rivera, B. Jensen, and R. Vanfleet, “SEM EDX Analysis of Sub-Micron Thin Oxide Scale on 316L Stainless Steel,” Microscopy and Microanalysis **30,** 545–546 (2024).

Index